Contents lists available at ScienceDirect

Nano Energy

journal homepage: www.elsevier.com/locate/nanoen

Communication

Wafer-scale synthesis of monolayer WSe₂: A multi-functional photocatalyst for efficient overall pure water splitting

Yongjie Wang[a,b], Songrui Zhao[b,d], Yichen Wang[b], David Arto Laleyan[a,b], Yuanpeng Wu[a,b], Bin Ouyang[c,e], Pengfei Ou[c], Jun Song[c], Zetian Mi[a,b,*]

[a] *Department of Electrical Engineering and Computer Science, University of Michigan, 1301 Beal Avenue, Ann Arbor, MI 48109, USA*
[b] *Department of Electrical and Computer Engineering, McGill University, 3480 University Street, Montreal, Quebec, Canada H3A 0E9*
[c] *Department of Mining and Materials Engineering, McGill University, 3610 University Street, Montreal, Quebec, Canada H3A 0C5*
[d] *College of Information Science and Electronic Engineering, Zhejiang University, 38 Zheda Road, Hangzhou, Zhejiang 310027, China*
[e] *Department of Materials Science and Engineering, University of California, 2607 Hearst Avenue, Berkeley, CA 94720, USA*

ARTICLE INFO

ABSTRACT

A multi-functional photocatalyst, that can combine the catalytic functions of water oxidation and proton reduction together with light harvesting capacity, is highly desired for low cost, high efficiency, and highly stable solar fuel production. Monolayer WSe₂, with a direct energy gap of ~ 1.65 eV is a nearly ideal light absorber to convert sunlight to hydrogen fuels through solar water splitting. To date, however, the controlled synthesis of monolayer WSe₂ on a wafer scale and the realization of overall water splitting on WSe₂ have remained elusive. Here, we report the van de Waals epitaxy of crystalline monolayer WSe₂ on large area amorphous SiOₓ substrates. We have demonstrated, for the first time, the multi-functionality of monolayer WSe₂ in solar water splitting, including extraordinary capacities for efficient light harvesting, water oxidation, and proton reduction. The absorbed photon conversion efficiency exceeds 12% for a single monolayer WSe₂. This work provides a viable strategy for wafer-scale synthesis of multi-functional photocatalysts for the development of efficient, low cost, and scalable solar fuel devices and systems.

1. Introduction

Solar water splitting, through the dissociation of water molecules to H_2 and O_2, is one significant step of artificial photosynthesis to solve future energy and environmental issues [1,2]. Critical to the development of an efficient solar water splitting cell is the integration of catalysts, for water oxidation and/or proton reduction, with the semiconductor light absorber. For practical applications, it is also essential that the catalysts are of low cost and are earth-abundant. Si and III-V semiconductor materials [3–7] have been extensively studied for solar-to-fuel conversion due to the efficient light absorption. However, their operation often requires the use of expensive noble metal catalysts and their performance suffers from serious photo-corrosion [3,4]. Moreover, the substrates to grow III-V semiconductors are prohibitively expensive, and it is extremely difficult to integrate III-V semiconductor light absorbers on low cost foreign substrates, due to the lattice mismatch related issues [8–10]. Additionally, previously reported photocatalysts, such as CoO_x, IrO_x, Pt, MoS_2, and RuO_x are only capable of either oxidizing water [2,10–12] or proton reduction [13–16]. To efficiently catalyze overall water splitting, the integration of dual catalysts with light absorbers is required. In such systems, charge carrier transport from the semiconductor light absorber to the catalyst is often hindered by the presence of impurities and/or potential barriers related to imperfect band alignment [17,18]. It has been envisioned that a multi-functional photocatalyst, that exhibit both catalytic and light harvesting capacities, can potentially address the challenges and performance bottlenecks of solar water splitting by minimizing the over-potential requirement, enhancing charge carrier transport and collection efficiency, and reducing the fabrication cost [2,10].

Recently, two-dimensional (2D) transitional metal dichalcogenides (TMDCs) have been intensively studied for electronic, optoelectronic, and solar energy device applications [19–23]. Among various TMDCs, monolayer WSe₂ has a direct bandgap of ~ 1.65 eV and can absorb visible light efficiently while promising a relatively large photovoltage. Even for a single monolayer, 1–5% light [24,25] can be absorbed for photons with energy above the bandgap. Significantly, the energy band edges of monolayer WSe₂ can straddle water redox reactions [26–29]: its conduction band edge is positioned slightly more negative than the

---

water reduction potential, while its valence band edge is located more positive than water oxidation potential and possess the capacity to drive oxygen evolution which is normally a bottleneck for water splitting. Previously, WSe$_2$ was used as a photoanode in iodate electrolytes [30–32]. Recent studies have shown that monolayer TMDC provides catalytic sites [13,33–35] at edges for water redox reaction, which was not significant in bulk TMDC materials, and hydrogen evolution reaction through TMDC 2D materials has been intensively studied [16,33,36]. To date, however, there have been no reports on overall water splitting on monolayer or few layers WSe$_2$, and their capacity for water oxidation has remained largely unknown [34]. This has been limited, in part, by the lack of controlled synthesis of large area TMDC atomic crystals. Recently, significant efforts have been devoted toward the large area growth of TMDC monolayers using chemical vapor deposition (CVD) and physical vapor deposition (PVD) [19,23,37–39], but with limited success.

To achieve scalable, low cost solar water splitting devices and systems, it is highly desired to integrate TMDC catalysts on nonconventional substrates, such as amorphous SiO$_x$ or metal substrates. In this work, by exploiting two-dimensional van der Waals (vdW) growth [21,29], we have investigated the molecular beam epitaxial (MBE) growth and structural, optical and photocatalytic characteristics of monolayer and multi-layer WSe$_2$ directly on amorphous SiO$_x$ templates. This is in direct contrast to previous MBE attempts of isolated TMDC flakes on crystalline substrates [29,40–43]. The vdW epitaxy of large area, uniform, and crystalline WSe$_2$ on amorphous substrates is unambiguously supported by the streaky reflection high-energy electron diffraction (RHEED) pattern, a widely used technique to distinguish single crystalline, polycrystalline, and amorphous structures during epitaxy, and by detailed transmission electron microscopy (TEM) studies. The formation of uniform, continuous WSe$_2$ monolayer on 2" SiO$_x$ templates is further confirmed by detailed optical studies, including photoluminescence (PL) and Raman mapping. We have further demonstrated that, through the seamless integration of catalytic properties with light harvesting capacity, monolayer WSe$_2$ can serve as a multi-functional photocatalyst and offer distinct advantages for solar water splitting, including significantly reduced over-potential, high efficiency, and stability.

2. Material and methods

2.1. Molecular beam epitaxial growth

WSe$_2$ monolayer, bilayer, and trilayer samples were grown on 250 nm SiO$_x$/Si substrates using a Veeco GENxplor MBE system. Prior to loading into the MBE chamber, SiO$_x$/Si substrates were first cleaned using acetone, methanol, and deionized water. During the growth of WSe$_2$, the substrate temperature was kept at ~ 400 °C. A standard effusion cell with PBN crucible and an e-bean evaporator are used for the thermal evaporation of Se and W sources, respectively. Se flux beam equivalent pressure was measured to be ~ 3.5×10^{-7} Torr; and W deposition rate was ~ 0.16 Å min^{-1}. The growth rate was estimated to be ~ 0.7 Å min^{-1} and it took ~ 11 min to synthesize one monolayer. Low substrate temperature and high selenium flux are chosen to ensure that tungsten atoms can be selenidized thoroughly. After growth with a desired thickness, substrate temperature was raised to 650 °C for 10-min annealing with continuous Se flux.

2.2. Characterizations

Reflection high-energy electron diffraction (RHEED, Staib Instruments) was used to monitor the layer-by-layer growth of WSe$_2$ nanostructures in situ. The beam acceleration voltage and filament current were set to 13.5 kV and 1.5 A, respectively. Micro-PL and micro-Raman studies were conducted using Renishaw inVia confocal Raman microscope with a 514 nm argon laser. The stoichiometric analysis was performed by X-ray photoelectron spectroscope (XPS,

Thermo Scientific K-Alpha) with Al-Kα monochromatic source (hν = 1486.6 eV) with a spot size of 400 µm. The microstructure and morphology were characterized by optical microscope (Olympus MX40), atomic force microscope (AFM, Bruker Multimode), and transmission electron microscope (TEM, FEI Tecnai G^2 F20). TEM operated at 200 kV with a point resolution of 0.25 nm with a built-in EDX equipment (Oxford Instruments).

PMMA-assisted transfer method was used to prepare samples for TEM imaging. PMMA supporting layer for handling WSe$_2$ film was first spin-coated on top of WSe$_2$ sample on SiO$_x$/Si substrates at 3000 rpm for 30 s, followed by a curing process at 160 °C for 10 min. PMMA-coated WSe$_2$ sample was then diced into small pieces and immersed into 1 M KOH solution. After one hour, KOH solution etched SiO$_x$ sublayer away making PMMA/WSe$_2$ film peel off from substrate and float on etchant surface. Subsequently, the detached PMMA/WSe$_2$ film was transferred into deionized water to remove etchant residues for several times. A TEM grid, or other substrates, was used to scoop it out from water surface. Then PMMA/WSe$_2$ film on new substrate was baked at 65 °C for two hours to enhance the adhesion. Finally, PMMA supporting layer was removed in acetone solution.

### 2.3. Solar water splitting measurements

WSe$_2$ monolayer samples were placed in a quartz chamber using polytetrafluoroethylene holders. 65 mL DI-water was added as reactant that had been pre-purged with argon gas for 30 min to remove the dissolved gases. Afterwards, the chamber was sealed with a transparent quartz cover by pumping down for 10 min. Before water splitting measurement, 1 mL gas sample was injected into a gas chromatograph machine (GC, Shimazdu, GC-8A) to ensure the chamber was in good vacuum. Then solar spectra (~ 2200 mW cm^{-2}) from Xenon lamp with AM1.5G filter was irradiated onto WSe$_2$ sample through the quartz lid, driving solar water splitting reactions on the surface of WSe$_2$ monolayer. After every 15 min, gas production from water splitting was analyzed by injecting 1 mL gas sampling into GC using a SGE syringe with valves. For half reaction experiments with sacrificial reagents, 13 mL CH$_3$OH with 52 mL DI-water and 65 mL 3 mM AgNO$_3$ solutions were added, respectively, for water reduction reaction with H$_2$ generation and water oxidation reaction with O$_2$ evolution.

3. Results and discussions

2D WSe$_2$ layers were grown on amorphous SiO$_x$ substrates using a Veeco GENxplor MBE system (see Section 2.1). The observation of streaky RHEED feature during vdW growth of monolayer WSe$_2$ film is shown in Fig. 1a, which provides unambiguous evidence for the achievement of crystalline WSe$_2$ directly on amorphous substrates with atomically smooth surface. Similar streaky RHEED feature was reported for WSe$_2$ epitaxy previously, but the growth took place on crystalline GaAs and graphite substrates [29,40–43]. Moreover, with the vdW interaction between WSe$_2$ layers [23,29], multilayer WSe$_2$ films can be directly synthesized on a wafer scale. Optical images of WSe$_2$ grown on SiO$_x$ are shown in Supplementary material Figs. S1 and S2 and RHEED observation of WSe$_2$ grown on sapphire is displayed in Supplementary material Fig. S3. Stoichiometric analysis of epitaxial WSe$_2$ was performed using high-resolution X-ray photoelectron spectroscopy (XPS), shown in Fig. 1b. The atomic percentage ratio of W and Se was measured to be ~ 1:2, suggesting the formation of nearly stoichiometric WSe$_2$. The absence of W and Se oxidation peaks confirms the high purity of epitaxial WSe$_2$. Elemental analysis of monolayer WSe$_2$ was further analyzed by energy dispersive X-ray spectroscopy (EDX) as shown in Supplementary material Fig. S4. A typical optical microscope image of monolayer WSe$_2$ grown on SiO$_x$ is shown in Fig. 1c, and its thickness was measured to be ~ 0.8 nm by atomic force microscopy (AFM).

PL and Raman footprint of 1–3 ML WSe$_2$ films are investigated to
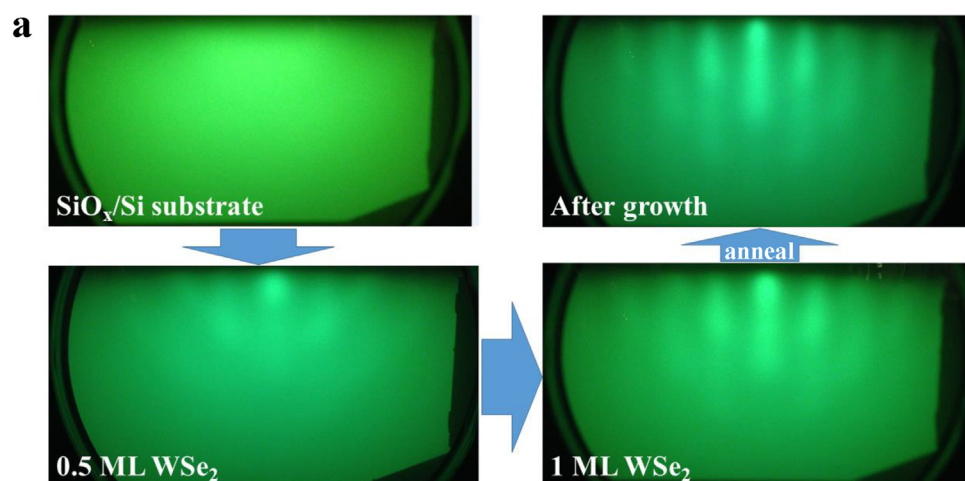
Fig. 1. Growth and characterization of monolayer WSe$_2$ directly grown on SiO$_x$ templates. (a) *In-situ* observation of RHEED patterns during MBE growth of WSe$_2$ monolayer on SiO$_x$/Si substrates. (b) XPS spectra of W and Se core-level peaks. The atomic percentage ratio of W and Se was determined to be $\sim$ 1:2. (c) Optical microscope image of bare SiO$_x$/Si substrate and as-grown WSe$_2$ monolayer sample; partial WSe$_2$ film was intentionally removed to expose SiO$_x$ surface. The insert is an AFM height measurement revealing its thickness of $\sim$ 0.8 nm corresponding to monolayer WSe$_2$ film.
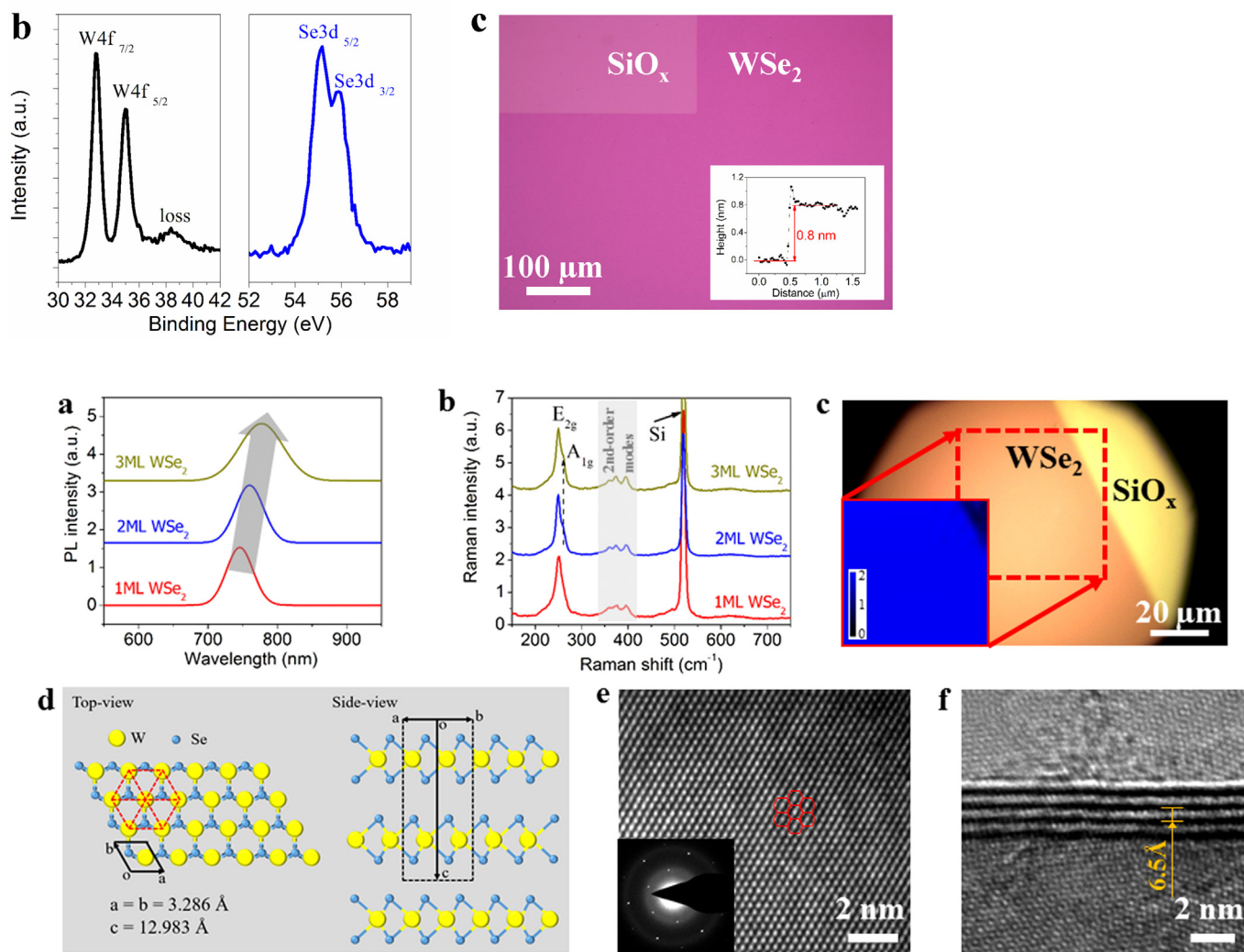
Fig. 2. Optical properties and crystal structures of 1–3 ML WSe$_2$ nanostructures. (a) Micro-photoluminescence spectra of 1–3 ML WSe$_2$; the gray arrow indicates the reduced energy gap of WSe$_2$ with increased thickness. (b) Micro-Raman spectra of 1–3 ML WSe$_2$ samples at room temperature; E$_{2g}$ peak at $\sim$ 250.8 cm^{-1} is the identification of WSe$_2$ crystals. (c) Raman mapping of E$_{2g}$ peak, in 50 μm × 50 μm region as labeled under optical microscope, where some material was deliberately removed to expose SiO$_x$ surface. (d) Schematic atomic configuration of 2H-WSe$_2$ crystal with layered structure. The dashed hexagon represents the distribution of tungsten atoms. (e) High-resolution plane-view TEM image of WSe$_2$ monolayer film. The insert corresponds to selected area electron diffraction pattern. The suspended solid hexagons in (e) represent W atomic distribution of 2H-WSe$_2$ crystal. (f) Lateral view of multilayer WSe$_2$ revealing its layer-by-layer stacking structure.

elucidate their optical properties. Fig. 2a compares the PL spectra of 1–3 ML WSe$_2$ samples measured at room temperature (R.T.). With increasing thickness, the energy bandgap, evidenced by the PL peak position [24,25,39,44], is reduced gradually. The relatively large full-width-at-half-maximum (FWHM, ~ 45 nm) is attributed to the inhomogeneous broadening associated with the presence of defects and grain boundaries. Shown in Fig. 2b are the Raman scattering spectra for WSe$_2$ samples with different thicknesses. One in-plane vibration mode E$_{2g}$ at ~ 250.8 cm^{-1} is observed for identifying WSe$_2$ nanostructures; the shoulder peak A$_{1g}$, representing out-of-plane vibration, at ~ 260.2 cm^{-1} is undetected in monolayer sample but is present in thicker layers [42,45]. There are also several weak modes at 350–400 cm^{-1} representing second-order vibration [39] for WSe$_2$ crystals. A typical Raman mapping of E$_{2g}$ scattering at ~ 250.8 cm^{-1} is shown in Fig. 2c. Some WSe$_2$ material was intentionally removed to expose SiO$_x$ surface for better observation under optical microscope.

Monolayer WSe$_2$ consists of three atom layers where W atom layer is sandwiched between two equivalent Se layers by forming interatomic covalent bonding [22,46]. The atomic structure [27,47] of 2H-phase WSe$_2$ crystal is schematically depicted in Fig. 2d. Tungsten atoms form face-centered hexagonal pattern [48] and only van der Waals force exists between layers. High-resolution transmission electron microscopy (HR-TEM) was utilized to observe its hexagonal symmetry and layer structure of WSe$_2$ sample, shown in Fig. 2e and f. The corresponding selected area electron diffraction (SAED) pattern within sixfold symmetry demonstrates that it is a monolayer crystal structure with a hexagonal lattice [22]. Red solid hexagons in Fig. 2e represent the atomic distribution of tungsten in WSe$_2$ crystal, which reflects a three-fold rotational symmetry in 2H phase. Recent studies have shown that the edge sites of 2H-phase TMDC are catalytically active [13,33]. In this study, during the MBE growth of WSe$_2$, a large number of edge sites are spontaneously formed, as shown in Supplementary material Fig. S5, which can provide catalytic functions [33–35]. Fig. 2f reveals the layer-by-layer growth of WSe$_2$ films. The interlayer spacing is determined to be ~ 0.65 nm for one WSe$_2$ layer, which is consistent with theoretical calculation and other experimental reports [23,25,29,37]. The atomically smooth layer structure further confirms the vdW epitaxy of WSe$_2$ grown on amorphous SiO$_x$ substrates by MBE. Light absorption property of WSe$_2$, as presented in Supplementary material Figs. S6 and S7, was examined by ultraviolet-visible spectrophotometry (UV–vis).

Previous studies have suggested that the band edges of monolayer WSe$_2$ straddles water redox reactions [26–29], schematically illustrated in Fig. 3a. However, it has remained unknown if monolayer WSe$_2$ possesses the capacity to spontaneously drive proton reduction and water oxidation under sunlight illumination. In this regard, we first performed H$_2$ and O$_2$ evolution half-reactions using sacrificial reagents CH$_3$OH and AgNO$_3$, respectively, shown in Fig. 3b and c. For the H$_2$ evolution half-reaction, CH$_3$OH is sacrificially oxidized by photo-generated holes in the valence band, and photo-generated electrons can reduce H$^+$ to H$_2$ at the catalytic edge sites of monolayer WSe$_2$. The continuous H$_2$ evolution under light illumination demonstrates the catalytic capability of proton reduction for monolayer WSe$_2$ without any other co-catalyst. For O$_2$ evolution half-reaction, H$_2$O molecule is oxidized to produce O$_2$ gas while the photo-excited electrons reduce Ag$^+$ to Ag. The continuous O$_2$ generation shown in Fig. 3c confirms the catalytic ability of water oxidation for monolayer WSe$_2$. In these studies, we have performed detailed control experiments on SiO$_x$/Si wafer without the presence of monolayer WSe$_2$, and no H$_2$ or O$_2$ production was measured within the experimental error. The continuous evolution of H$_2$ and O$_2$, shown in Fig. 3b and c, therefore suggests that the conduction and valence band edges of monolayer WSe$_2$ meet the thermodynamic and kinetic requirements for solar water splitting. This is somewhat surprising, given the relatively narrow energy bandgap (~ 1.65 eV) of monolayer WSe$_2$ and small overpotential for proton reduction (~ 0.1 eV) and water oxidation (~ 0.3 eV), shown in Fig. 3a. However, in monolayer WSe$_2$ photocatalyst, charge carrier

generation via photoexcitation and catalytic reaction take place approximately at the same location. As such, photoexcited high-energy electrons and holes can possibly drive proton reduction and water oxidation before cooling to excitons. The resulting hot carrier effect can significantly enhance the photocatalytic activity, which has been reported previously [48–51]. In addition, being in close proximity for the key steps in water splitting reaction, including photoexcitation, charge carrier generation and extraction, and catalytic reaction may enhance the thermodynamic and kinetic coupling of sequential reactions at the nanoscale, which has been a topic being intensively investigated [52–54].

We have subsequently investigated overall solar water splitting on monolayer WSe$_2$ in pure water (see Section 2.3). Shown in Fig. 3d, the H$_2$/O$_2$ evolution ratio is nearly stoichiometric, in the range of 1.95–2.1, confirming the reaction is direct water splitting. H$_2$ generation rate is measured to be ~ 48.4 μmol h^{-1} cm^{-2} corresponding to ~ 0.145% solar-to-hydrogen (STH) conversion efficiency and ~ 12.3% absorbed photon conversion efficiency (APCE). Detailed calculations are shown in Supplementary material Note S8. It is noticed that the photon-to-electron conversion efficiency may be limited by non-radiative recombination, due to the presence of defects [55,56]. The reported solar-to-hydrogen conversion efficiency of ~ 0.145% on monolayer WSe$_2$ is compared favorably with the maximum power conversion efficiency (~ 0.2%) of WSe$_2$-MoSe$_2$ and WSe$_2$-WSe$_2$ p-n junctions reported previously [37,46]. The turnover number, defined as the ratio of the total amount of gas evolved (143 μmol cm^{-2} for H$_2$ and O$_2$) to the amount of WSe$_2$ photocatalyst material (1.75×10^{-3} μmol cm^{-2}), exceeded 80,000 during the course of ~ 2 h of pure water splitting. We have further investigated the variation of STH efficiency for overall pure water splitting on monolayer WSe$_2$ as a function of light intensity. Shown in Supplementary material Fig. S8, STH efficiency showed an increasing trend with increasing light intensity, possibly due to the reduced nonradiative recombination at high carrier densities. Similar trends have also been observed in overall pure water splitting on nanowire structures [1]. Finally, when normalized by the volume and mass of the WSe$_2$ photocatalyst material, the H$_2$ production rates are estimated to be ~ 18,370 L h^{-1} cm^{-3} and 1972 L h^{-1} g^{-1}, respectively, shown in Supplementary material Fig. S9, which are more than 50 times higher compared to previously best reported photocatalyst (1.6 L h^{-1} g^{-1} under 100 mW cm^{-2} light) for CoO nanoparticles [57]. As shown in Supplementary material Fig. S10, similar photocatalytic results were also observed for monolayer WSe$_2$ grown on sapphire substrate. In these studies, careful control experiments were performed on both SiO$_x$/Si and sapphire without the presence of monolayer WSe$_2$, which did not show any H$_2$ or O$_2$ evolution. In addition, Rh/Cr$_2$O$_3$/CoO$_x$ nanoparticles as cocatalysts did not significantly improve the photocatalytic performance of monolayer WSe$_2$, which could be partly due to the light blocking effect of the co-catalysts. Illustrated in Supplementary material Fig. S10, we have also performed overall water splitting experiments on 2 ML and 3 ML WSe$_2$ samples, which, however, exhibit negligible photocatalytic activity, possibly due unsuited energy band alignment for overall water splitting with increasing thicknesses. Photocatalytic stability of 1 ML WSe$_2$ samples for overall pure water splitting was further studied. There is no significant change of both H$_2$ and O$_2$ gas production rate over 8 h, shown in Supplementary material Fig. S11, which suggests that monolayer WSe$_2$ exhibits a high level of stability. In addition, Raman spectra of 1 ML WSe$_2$ sample before and after pure water splitting experiments were conducted, as shown in Supplementary Fig. S12, which are nearly identical, indicating monolayer WSe$_2$ was stable during pure water splitting experiments. As listed in Supplementary material Table S1, the photocatalytic performance of 1 ML WSe$_2$ was further compared to some previously reported semiconductors for pure water splitting experiments. It is seen that the normalized H$_2$ evolution rate (L h^{-1} g^{-1}) is orders of magnitude higher than previously reported values, showing the extraordinary potential of monolayer materials for solar fuel production.
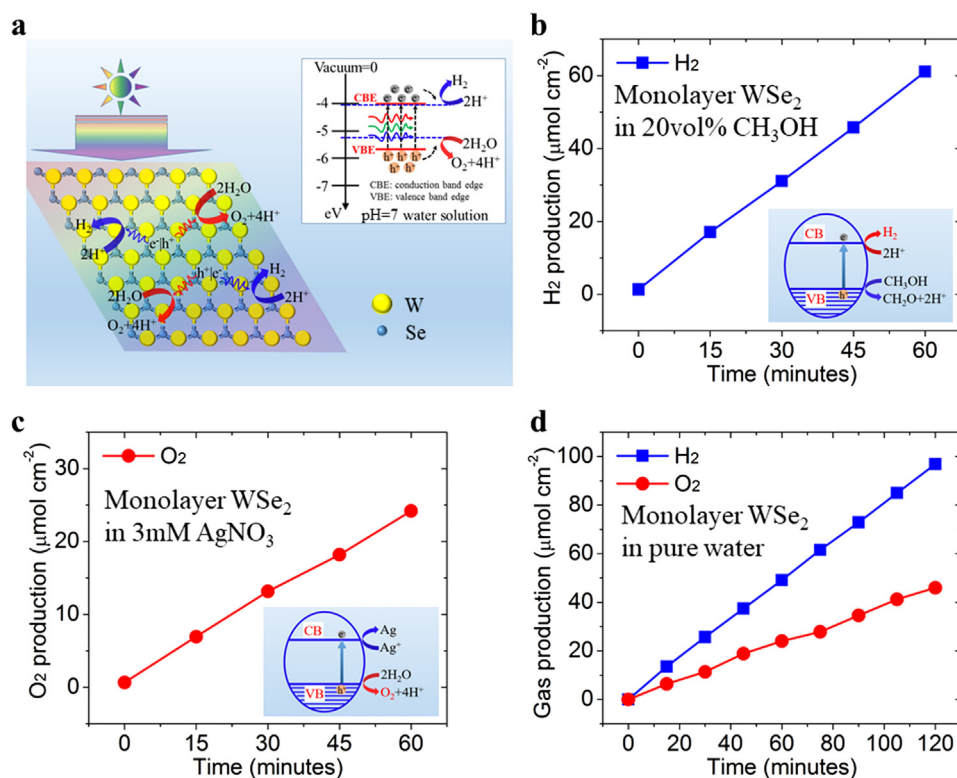
Fig. 3. Solar water splitting measurements of MBE-grown multi-functional monolayer WSe_2 photocatalyst. (a) Schematic illustration of overall water splitting reaction on monolayer WSe_2 without incorporating any co-catalyst. Inset: conduction and valence band edge positions vs. water reduction and water oxidation reactions in pH = 7 water solution. (b) H_2 and (c) O_2 evolution half reactions in the presence of sacrificial reagents, methanol and silver nitrate solutions, respectively, over monolayer WSe_2 under a 300 W full arc xenon lamp illumination with an AM 1.5G filter. (d) Overall photocatalytic water splitting on monolayer WSe_2 under a 300 W xenon lamp irradiation with an AM1.5G optical filter. No degradation of the photocatalytic activity was observed during the course of the reaction.

4. Conclusion

In summary, we have demonstrated the multifunctionality of monolayer WSe_2 in solar water splitting, including extraordinary capacities for efficient light harvesting, water oxidation, and proton reduction. The absorbed photon conversion efficiency exceeds 12% for a single monolayer WSe_2. We have shown that wafer-scale WSe_2 monolayer sample could be directly grow on amorphous substrates by MBE with precise layer control and can exhibit superb optical properties and catalytic performance. This work provides a viable strategy for wafer-scale synthesis of multi-functional photocatalysts for the development of efficient, low cost, and scalable solar fuel devices and systems.

Acknowledgements

Conflict of interest

The authors declare no competing financial interests.

Appendix A. Supplementary material

Optical images of WSe_2 on SiO_x/Si substrates, RHEED pattern during WSe_2 growth on sapphire substrate, EDX, low-magnification TEM, and light absorption characterizations of monolayer WSe_2, efficiency calculations, normalized hydrogen production, control experiments, stability study, Raman spectra after experiment, and photocatalytic performance comparison with other semiconductors.

Supplementary data associated with this article can be found in the online version at http://dx.doi.org/10.1016/j.nanoen.2018.06.047.

References

[1] M.G. Kibria, F.A. Chowdhury, S. Zhao, B. AlOtaibi, M.L. Trudeau, H. Guo, Z. Mi, Nat. Commun. 6 (2015) 6797.

[2] J. Yang, J.K. Cooper, F.M. Toma, K.A. Walczak, M. Favaro, J.W. Beeman, L.H. Hess, C. Wang, C. Zhu, S. Gul, J. Yano, C. Kisielowski, A. Schwartzberg, I.D. Sharp, Nat. Mater. 16 (2017) 335–341.

[3] O. Khaselev, J.A. Turner, Science 280 (1998) 425.

[4] S. Hu, M.R. Shaner, J.A. Beardslee, M. Lichterman, B.S. Brunschwig, N.S. Lewis, Science 344 (2014) 1005.

[5] M.G. Kibria, Z. Mi, J. Mater. Chem. A 4 (2016) 2801–2820.

[6] S.Y. Reece, J.A. Hamel, K. Sung, T.D. Jarvi, A.J. Esswein, J.J.H. Pijpers, D.G. Nocera, Science 334 (2011) 645.

[7] D. Liu, L. Li, Y. Gao, C. Wang, J. Jiang, Y. Xiong, Angew. Chem. Int. Ed. 54 (2015) 2980–2985.

[8] M. Yamaguchi, T. Takamoto, K. Araki, N. Ekins-Daukes, Sol. Energy 79 (2005) 78–85.

[9] K. Chen, R. Kapadia, A. Harker, S. Desai, J. Seuk Kang, S. Chuang, M. Tosun, C.M. Sutter-Fella, M. Tsang, Y. Zeng, D. Kiriya, J. Hazra, S.R. Madhvapathy, M. Hettick, Y.-Z. Chen, J. Mastandrea, M. Amani, S. Cabrini, Y.L. Chueh, J.W. Ager Iii, D.C. Chrzan, A. Javey, Nat. Commun. 7 (2016) 10502.

[10] D. Kang, J.L. Young, H. Lim, W.E. Klein, H. Chen, Y. Xi, B. Gai, T.G. Deutsch, J. Yoon, Nat. Energy 2 (2017) 17043.

[11] M.G. Kibria, H.P.T. Nguyen, K. Cui, S. Zhao, D. Liu, H. Guo, M.L. Trudeau, S. Paradis, A.R. Hakima, Z. Mi, ACS Nano 7 (2013) 7886–7893.

[12] H.B. Yang, J. Miao, S.F. Hung, F. Huo, H.M. Chen, B. Liu, ACS Nano 8 (2014) 10403–10413.

[13] G. Ye, Y. Gong, J. Lin, B. Li, Y. He, S.T. Pantelides, W. Zhou, R. Vajtai, P.M. Ajayan, Nano Lett. 16 (2016) 1097–1103.

[14] J. Luo, L. Steier, M.K. Son, M. Schreier, M.T. Mayer, M. Grätzel, Nano Lett. 16 (2016) 1848–1857.

[15] S. Fan, B. AlOtaibi, S.Y. Woo, Y. Wang, G.A. Botton, Z. Mi, Nano Lett. 15 (2015) 2721–2726.

[16] J.R. McKone, A.P. Pieterick, H.B. Gray, N.S. Lewis, J. Am. Chem. Soc. 135 (2013) 223–231.

[17] M.G. Walter, E.L. Warren, J.R. McKone, S.W. Boettcher, Q. Mi, E.A. Santori,

N.S. Lewis, Chem. Rev. 110 (2010) 6446–6473.

[18] R.M. Navarro Yerga, M.C. Álvarez Galván, F. del Valle, J.A. Villoria de la Mano, J.L.G. Fierro, ChemSusChem 2 (2009) 471–485.

[19] X. Duan, C. Wang, J.C. Shaw, R. Cheng, Y. Chen, H. Li, X. Wu, Y. Tang, Q. Zhang, A. Pan, J. Jiang, R. Yu, Y. Huang, X. Duan, Nat. Nanotechnol. 9 (2014) 1024–1030.

[20] J. Feng, X. Qian, C.W. Huang, J. Li, Nat. Photonics 6 (2012) 866–872.

[21] K.S. Novoselov, A. Mishchenko, A. Carvalho, A.H. Castro Neto, Science 353 (2016) aac9439.

[22] C. Huang, S. Wu, A.M. Sanchez, J.J.P. Peters, R. Beanland, J.S. Ross, P. Rivera, W. Yao, D.H. Cobden, X. Xu, Nat. Mater. 13 (2014) 1096–1101.

[23] K. Chen, X. Wan, J. Xu, Adv. Funct. Mater. 27 (2017) 1603884.

[24] J.S. Ross, P. Klement, A.M. Jones, N.J. Ghimire, J. Yan, D.G. Mandrus, T. Taniguchi, K. Watanabe, K. Kitamura, W. Yao, D.H. Cobden, X. Xu, Nat. Nanotechnol. 9 (2014) 268–272.

[25] A. Pospischil, M.M. Furchi, T. Mueller, Nat. Nanotechnol. 9 (2014) 257–261.

[26] S. McDonnell, A. Azcatl, R. Addou, C. Gong, C. Battaglia, S. Chuang, K. Cho, A. Javey, R.M. Wallace, ACS Nano 8 (2014) 6265–6272.

[27] W. Liu, J. Kang, D. Sarkar, Y. Khatami, D. Jena, K. Banerjee, Nano Lett. 13 (2013) 1983–1990.

[28] M.S. Christopher, A. Rafik, M. Stephen, L.H. Christopher, M.W. Robert, 2D Mater. 4 (2017) 025084.

[29] S. Vishwanath, X. Liu, S. Rouvimov, L. Basile, N. Lu, A. Azcatl, K. Magno, R.M. Wallace, M. Kim, J.C. Idrobo, J.K. Furdyna, D. Jena, H.G. Xing, J. Mater. Res. 31 (2016) 900–910.

[30] G. Kline, K. Kam, D. Canfield, B.A. Parkinson, Sol. Energy Mater. 4 (1981) 301–308.

[31] R. Tenne, A. Wold, Appl. Phys. Lett. 47 (1985) 707–709.

[32] R. Bourezg, G. Couturier, J. Salardenne, F. Lévy, Phys. Rev. B 46 (1992) 15404–15410.

[33] X. Yu, M.S. Prevot, N. Guijarro, K. Sivula, Nat. Commun. 6 (2015) 7596.

[34] P. Karfa, R. Madhuri, P.K. Sharma, J. Mater. Chem. A 5 (2017) 1495–1508.

[35] Y. Ouyang, C. Ling, Q. Chen, Z. Wang, L. Shi, J. Wang, Chem. Mater. 28 (2016) 4390–4396.

[36] H. Wang, D. Kong, P. Johanes, J.J. Cha, G. Zheng, K. Yan, N. Liu, Y. Cui, Nano Lett. 13 (2013) 3426–3433.

[37] M.Y. Li, Y. Shi, C.C. Cheng, L.S. Lu, Y.C. Lin, H.L. Tang, M.L. Tsai, C.W. Chu, K.H. Wei, J.H. He, W.H. Chang, K. Suenaga, L.J. Li, Science 349 (2015) 524–528.

[38] A. Neumann, J. Lindlau, L. Colombier, M. Nutz, S. Najmaei, J. Lou, A.D. Mohite, H. Yamaguchi, A. Högele, Nat. Nanotechnol. 12 (2017) 329–334.

[39] B. Liu, M. Fathi, L. Chen, A. Abbas, Y. Ma, C. Zhou, ACS Nano 9 (2015) 6119–6127.

[40] S.M. Poh, S.J. Tan, X. Zhao, Z. Chen, I. Abdelwahab, D. Fu, H. Xu, Y. Bao, W. Zhou, K.P. Loh, Adv. Mater. 12 (2017) 1605641.

[41] O. Koji, K. Aleksandra, A.E.N. Ryan, M. Fumihiko, K. Kazuhide, Y. Hideki, Appl. Phys. Express 9 (2016) 115501.

[42] K.E. Aretouli, D. Tsoutsou, P. Tsipas, J. Marquez-Velasco, S. Aminalragia Giamini, N. Kelaidis, V. Psycharis, A. Dimoulas, ACS Appl. Mater. Interfaces 8 (2016) 23222–23229.

[43] V. Suresh, L. Xinyu, R. Sergei, C.M. Patrick, A. Angelica, M. Stephen, M.W. Robert, M.F. Randall, K.F. Jacek, J. Debdeep, X. Huili Grace, 2D Mater. 2 (2015) 024007.

[44] D.H. Lien, J.S. Kang, M. Amani, K. Chen, M. Tosun, H.P. Wang, T. Roy, M.S. Eggleston, M.C. Wu, M. Dubey, S.C. Lee, J.H. He, A. Javey, Nano Lett. 15 (2015) 1356–1361.

[45] J. Lu, A. Carvalho, H. Liu, S.X. Lim, A.H. Castro Neto, C.H. Sow, Angew. Chem. Int. Ed. 55 (2016) 11945–11949.

[46] B.W.H. Baugher, H.O.H. Churchill, Y. Yang, P. Jarillo-Herrero, Nat. Nanotechnol. 9 (2014) 262–267.

[47] W. Wong-Ng, H.F. McMurdie, B. Paretzkin, Y. Zhang, K.L. Davis, C.R. Hubbard, A. Dragoo, J.M. Stewart, Powder Diffr. 2 (2013) 257–265.

[48] K. Tennakone, J. Bandara, Appl. Catal. A Gen. 208 (2001) 335–341.

[49] Y. Dong, J. Choi, H.K. Jeong, D.H. Son, J. Am. Chem. Soc. 137 (2015) 5549–5554.

[50] P. Sippel, W. Albrecht, D. Mitoraj, R. Eichberger, T. Hannappel, D. Vanmaekelbergh, Nano Lett. 13 (2013) 1655–1661.

[51] X. Fu, M. Xie, P. Luan, L. Jing, ACS Appl. Mater. Interfaces 6 (2014) 18550–18557.

[52] C. Li, S. Wang, T. Wang, Y. Wei, P. Zhang, J. Gong, Small 10 (2014) 2783–2790.

[53] F.E. Osterloh, Chem. Soc. Rev. 42 (2013) 2294.

[54] B. Wu, N. Zheng, Nano Today 8 (2013) 168–197.

[55] M. Danovich, V. Zolyomi, V.I. Fal'ko, I.L. Aleiner, 2D Mater. 3 (2016) 035011.

[56] W.T. Hsu, Y.L. Chen, C.H. Chen, P.S. Liu, T.H. Hou, L.J. Li, W.H. Chang, Nat. Commun. 6 (2015) 8963.

[57] L. Liao, Q. Zhang, Z. Su, Z. Zhao, Y. Wang, Y. Li, X. Lu, D. Wei, G. Feng, Q. Yu, X. Cai, J. Zhao, Z. Ren, H. Fang, F. Robles-Hernandez, S. Baldelli, J. Bao, Nat. Nanotechnol. 9 (2014) 69–73.

Yongjie Wang is a Ph.D. student in Electrical and Computer Engineering at the University of Michigan. He received his B.E. degree in 2012 from Composite Materials and Engineering, Harbin Institute of Technology, China, and M.S. degree from the University of California in 2014. His current research focuses on photocatalytic and photoelectrochemical water splitting on III-nitride and TMDC nanostructures.

Songrui Zhao is currently an Assistant Professor in College of Information Science and Electronic Engineering, Zhejiang University, China. He received Ph.D. degree in Electrical Engineering from McGill University in 2013. His research interests include molecular beam epitaxy of semiconductor nanostructures and optoelectronic devices.

Yichen Wang is a Postdoc researcher in the Department of Electrical and Computer Engineering at McGill University. He received his Ph.D. degree of Analytical Chemistry in 2014 from the University of Chinese Academy of Sciences. He is interested in the areas of metal and semiconductor nanomaterials fabrication, and their applications towards photo-, electro- and photoelectron-catalysis of water splitting and CO_2 reduction.

David Arto Laleyan is a Ph.D. student in Electrical and Computer Engineering at the University of Michigan, Ann Arbor. He received his Bachelor of Engineering degree in 2015 from McGill University (Montreal, Canada). His current research focuses on the epitaxial growth of III-nitride and two dimensional electronic and optoelectronic materials.
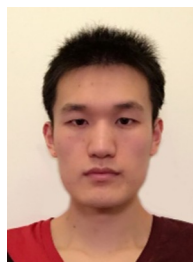
Yuanpeng Wu is a Ph.D. student in Electrical and Computer Engineering at the University of Michigan, Ann Arbor. He received his B.S. degree in 2012 from Shanxi University and M.E. degree from Zhejiang University in 2015 in China. His current research focuses on III-nitride nanostructure growth, characterization and high performance deep UV optoelectronic devices.

Bin Ouyang is a postdoctoral research associate working in University of California Berkeley. He received his B.Eng. in Materials Science and Engineering at Central South University in Changsha, China. After which he obtained his Ph.D. degree at McGill University in Montreal, Canada. His research focus is on theoretical understanding of phase transitions, thermodynamics and kinetics within solids.
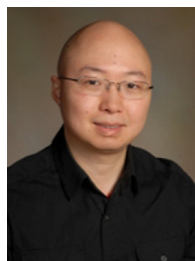
Jun Song is an Associate Professor in the Department of Mining and Materials Engineering at McGill University. He received his B.S degree in Mechanical Engineering from the University of Science and Technology of China on June 2003, and his Ph.D. degree in Mechanical & Aerospace Engineering from Princeton University on August 2008. His current research focuses on multiscale modeling and simulations of the mechanics and physics of nanoscale materials.
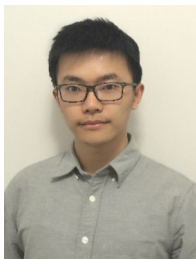
Pengfei Ou is a Ph.D. student in the Department of Mining and Materials Engineering at McGill University. He received his B.E. degree in Materials Science and Engineering from Central South University on June 2012, and M.E. degree in Materials Physics and Chemistry on May 2015 from Central South University. His current research focuses on theoretical modeling and simulations of electrocatalysis and electrochemical CO_2 reduction and water splitting on two-dimensional materials.

Zetian Mi is a Professor in the Department of Electrical Engineering and Computer Science at the University of Michigan. He received his Ph.D. in Applied Physics from the University of Michigan in 2006. His research interests are in the areas of III-nitride semiconductors, low dimensional nanostructures, LEDs, lasers, Si photonics, and solar fuels. He has received the Young Scientist Award from the Int. Symp. on Compound Semiconductors and the Young Investigator Award from the 27th North American Molecular Beam Epitaxy Conference. He is a Fellow of SPIE and OSA.